



Drug-Loaded Acoustic Nanodroplet for Dual-Imaging Guided Highly Efficient Chemotherapy Against Nasopharyngeal Carcinoma

Dayan Yang ^{*}, Qiqing Chen^{*}, Min Zhang, Guiying Feng, Dandan Sun, Ling Lin, Xiangxiang Jing 

Department of Ultrasonography, Hainan General Hospital/Hainan Affiliated Hospital of Hainan Medical University, Hainan, People's Republic of China

^{*}These authors contributed equally to this work

Correspondence: Ling Lin, Tel +86-8-9868642515, Email 13876673666@163.com; Xiangxiang Jing, Email ljxx2000@126.com

Background: Chemotherapy is an important approach to treating nasopharyngeal carcinoma (NPC). Unfortunately, the lack of selectivity, insufficient tumor accumulation, uneven tumor distribution and severe systemic toxicity lead to the unsatisfactory performance of these drugs. While a more precise drug delivery, on-demand drug release, and deep diffusion of drugs (homogeneous distribution of drugs in the tumor) could improve the application, they remain challenging. Chemotherapeutic drug-loaded acoustic nanodroplet with dual-imaging capacity is expected to solve these problems.

Methods: Folate (Fa)-modified and doxorubicin (Dox)-loaded acoustic poly (lactic-co-glycolic acid) (PLGA), low intensity focused ultrasound (LIFU)-responsive perfluoropentane (PFP) and Fe₃O₄ nanoparticles (designated as Fa-Fe@P-PFP-Dox) were integrated by a double-emulsion method. After the synthesis, the LIFU-triggered acoustic droplet vaporization (ADV) effect, LIFU-triggered drug release, cell targeting capability, in vitro cell-killing effects, biodistribution, PA/MR dual imaging (PA: photoacoustic; MR: magnetic resonance), LIFU-augmented Dox distribution in tumors and chemotherapeutic efficacy of Fa-Fe@P-PFP-Dox were investigated.

Results: The distribution of these drug-loaded nanodroplets was clearly monitored via PA/MR dual imaging. Upon LIFU irradiation, PFP within the Fa-Fe@P-PFP-Dox nanodroplets underwent ADV, which led to the release of Dox and promoted the deep penetration of Dox in tumor tissue, eventually achieving highly efficient chemotherapy against NPC. As a result, LIFU-triggered chemotherapy exerted a highly efficient therapeutic effect with a tumor inhibition rate of $74.24 \pm 7.95\%$.

Conclusion: Fa-modified and drug-loaded acoustic nanodroplets have been successfully constructed for dual-imaging guided highly efficient chemotherapy against NPC. This novel tumor drug delivery method is expected to provide an efficient, visualized, and precise personalized treatment method for NPC patients with minimal side effects.

Keywords: nasopharyngeal carcinoma, drug delivery, low intensity focused ultrasound, chemotherapy, deep penetration

Introduction

Nasopharyngeal carcinoma (NPC) is a malignant tumor that occurs in the nasopharyngeal cavity or upper throat, ranking top in both incidence and mortality out of all head-and-neck tumors.¹ And most NPC patients tend to present at an advanced stage, since the anatomical sites and the early symptoms of NPC were not obvious.² Currently, radiotherapy and chemotherapy are the main clinical therapeutic modalities for NPC.^{3,4} For patients with advanced NPC, the outcome of radiation therapy is usually not satisfactory, and the 5-year survival rate is only 50%.⁵ Chemotherapy is an important part of the comprehensive treatment of NPC.^{6,7} After intravenous administration, conventional chemotherapeutic drugs can be distributed throughout the whole body with poorly targeted tumor specificity.⁸ As a result, in order to ensure the therapeutic efficacy of chemotherapy, a larger dose of drugs is used, which will inevitably cause systemic toxicity (eg, organ dysfunction and bone marrow suppression).⁹ Understandably, targeting chemotherapeutic drugs directly at the tumor sites would significantly increase the therapeutic efficacy and reduce side effects.^{10,11}

With the advancement of molecular biology, people have a better understanding of the molecular mechanism of tumor occurrence, progression, and metastasis.¹² Along with the development, a new concept, tumor(-specific)-molecular targeted cancer therapy emerged.^{12–14} Previous studies have found that folate (Fa) receptors are overexpressed on the surface of malignant tumor cells (eg, ovarian cancer, cervical cancer, non-small cell lung cancer), while the expression is highly conserved in normal tissue cells.¹⁵ The higher expression of Fa receptors in tumor tissues lays the foundation for targeted therapy of malignant tumors.^{16,17} In one of the malignant tumor scenarios, detected by immunohistochemistry, the fresh NPC tissues were also found that the FA receptors were significantly highly expressed, with a positive rate of 85%, and nearly half of them were strongly positive.¹⁸ Consistent with the analysis of clinicopathological data, it was found that NPC with advanced clinical stages had a higher positive rate of Fa receptors.¹⁸ Therefore, it is logical to take advantage of the excessive Fa receptor as a target molecule. Moreover, Fa has the advantages of high affinity, small molecular weight, good stability, and low cost, which makes Fa receptor a promising target against advanced NPC.¹⁹

The delivery precision and efficacy are two of many challenges in the design of the molecule-targeted strategy.^{20,21} Engineered microbubbles are known to be responsive to ultrasound-targeted microbubble destruction (UTMD) technology, which can be used as a switch for drug release.^{22,23} Upon an enhanced delivery precision, the targeted organ could receive a significantly higher drug concentration.^{22,23} However, the tumor capillary endothelial space is only 100–780 nm, which forms a barrier that microbubbles can be too large to cross.^{24,25} Fortunately, it has been reported that perfluorocarbon-containing nanodroplets can undergo phase transitions through the acoustic droplet vaporization (ADV) effect, where the droplets can be enlarged from nanosize into microscale.^{26,27} The planned transformation would then enable an intelligent drug delivery, which circumvents the size limit of the vascular endothelial space and reaches the tumor area more efficiently.^{28,29} Upon low intensity focused ultrasound (LIFU) irradiation, the drug-loaded nanodroplets grow larger until burst and release the loaded drugs.^{28,29} In the meantime, it has been reported that UTMD could dilate the vascular endothelial space, which could be beneficial considering the high interstitial pressure, dense tumor mix, and other complications in the tumor environment.^{22,23} We expect that nanodroplets combined with LIFU irradiation can also achieve a similar effect, thereby promoting the drugs in the blood circulation to enter the tumor tissue through the dilated vascular endothelial space. The accumulation will in turn result in an enhanced release, thus strengthening the therapeutic effect. Besides, the high interstitial pressure and dense tumor matrix are also major obstacles for drugs to enter the inner tumor tissues.^{30,31} Drawing on UTMD technology to dilate the vascular endothelial space, the blast effect induced by nanodroplets combined with LIFU irradiation may destroy the barriers, allowing the drug to penetrate away from the blood vessels.³²

In order to monitor the distribution of drug-loaded nanodroplets in the tumor, it is necessary to incorporate imaging capabilities in these nanodroplets.^{33–35} Magnetic resonance (MR) imaging is a non-ionizing diagnostic imaging modality that utilizes strong magnetic fields and radiofrequency pulses to generate high-resolution images of anatomical structures.^{36,37} However, the sensitivity of MR imaging is relatively low.³⁸ Photoacoustic (PA) imaging, an emerging medical imaging technique, combines the high contrast and sensitivity of optical imaging with the tissue penetration depths of ultrasound (US), showing great potential for biomedical imaging applications.^{39,40} Therefore, to achieve precise tumor imaging, an ideal approach is to incorporate photoacoustic and MR contrast agents on one nanocarrier for MR/PA dual-modal imaging-guided delivery of chemotherapeutic drugs. Fe₃O₄ nanoparticles, an excellent contrast agent for MR/PA imaging,^{41,42} will be integrated into drug-loaded nanodroplets for monitoring the therapeutic process.

In this study, we rationally constructed Fa-modified and drug-loaded acoustic nanodroplets for dual-imaging guided highly efficient chemotherapy against NPC (Figure 1). Fa-modified poly (lactic-co-glycolic acid) (PLGA) is used as a carrier to load doxorubicin (Dox), a typical chemotherapeutic drug, and LIFU-responsive perfluoropentane (PFP) within the core, and Fe₃O₄ nanoparticles in the shell (designated as Fa-Fe@P-PFP-Dox). These Fa-Fe@P-PFP-Dox can readily accumulate in NPC tumor regions with the guidance of Fa, which can be monitored by PA/MR dual-modal imaging. Upon LIFU irradiation, PFP within droplets undergoes ADV, releasing Dox and promoting the deep penetration of Dox in tumor tissue, achieving highly efficient chemotherapy against NPC. This novel tumor drug delivery method is expected to provide an efficient, visualized, and precise treatment with minimal side effects.

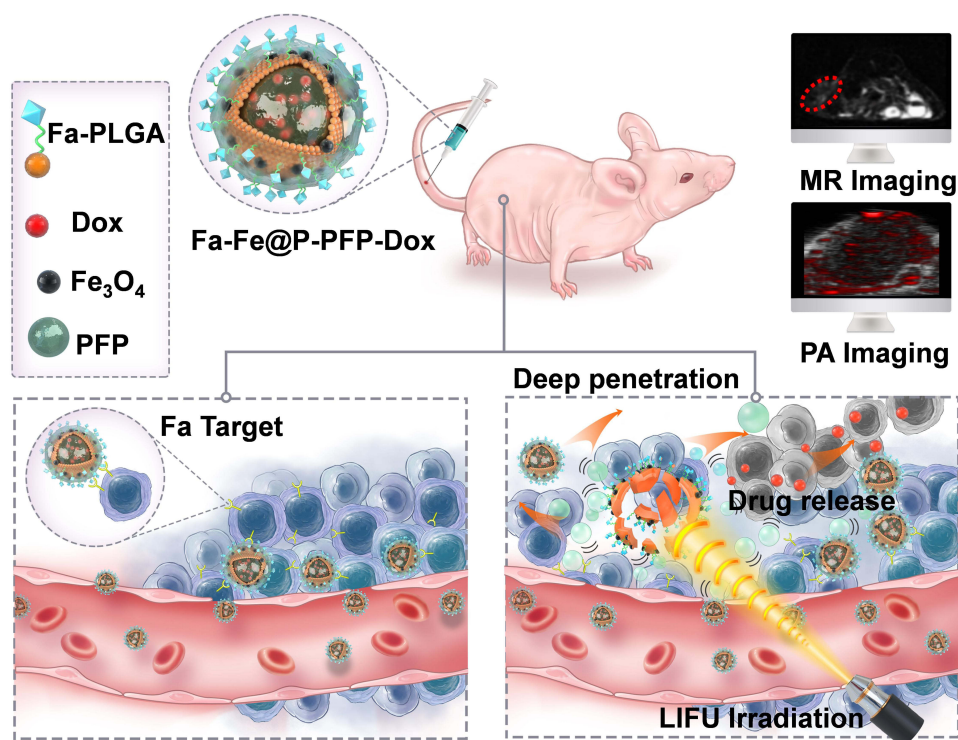


Figure 1 Schematic diagram of the structure of Fa-Fe@P-PFP-Dox nanodroplets and schematic illustration of the theranostic functions of the drug-loaded acoustic nanodroplets for dual-imaging guided highly efficient chemotherapy against nasopharyngeal carcinoma, including FA-mediated targeting capability, ADV-augmented deep penetration of Dox, and guidance/monitoring by dual-modal (PA and MR) imaging.

Materials and Methods

Materials

PLGA-PEG3.4k and Fa-PLGA-PEG3.4k were purchased from Xi'an Ruixi Biotechnology Co., Ltd (Xi'an, China). PFP and polyvinyl alcohol (PVA) were obtained from Sigma-Aldrich (St. Louis, MO, USA). Doxorubicin hydrochloride (Dox) was purchased from J&K Scientific Biotechnology Co., Ltd (Beijing, China). Oleic acid-stabilized iron oxide (Fe_3O_4) nanoparticles were purchased from Ocean Nano Tech, Inc. (AR, USA). 1,1'-dioctadecyl-3,3,3',3'-tetramethylindotricarbocyanine iodide (DIR) was purchased from Amy Jet Scientific Inc. (Wuhan, China). CCK-8 kits were purchased from Dojindo (Japan). Dichloromethane (CH_2Cl_2) was purchased from Aladdin (Shanghai, China).

Synthesis of Fa-Fe@P-PFP-Dox

Fa-Fe@P-PFP-Dox was fabricated according to a double emulsion method (water/oil/water, W/O/W).⁴³ Briefly, 50 mg of Fa-PLGA-PEG3.4k was dissolved in 2 mL of CH_2Cl_2 , followed by the addition of 150 μL oleic acid-stabilized Fe_3O_4 . Then, 150 μL of PFP and 10 mg of Dox were mixed with the dichloromethane mixture and undergo an ultrasonic process (100 W, 2.5 min) to obtain emulsion (W/O). After that, 5 mL of PVA was added to the above emulsion for the second ultrasonic treatment at the same power intensity (O/W). To fully volatilize the CH_2Cl_2 , 5 mL of 2% isopropanol was added to the obtained emulsion, the mixture was then mechanically stirred for 5 h in an ice bath. After centrifugation (10,000 rpm, 5 min), the Fa-Fe@P-PFP-Dox slurry was obtained for the following experiments. The fabrication procedure of Fa-Fe@P-PFP-Dox was identical to the Fa-Fe@P-PFP-Dox except that Fa-PLGA-PEG3.4k was replaced by PLGA-PEG3.4k.

Characterization of Fa-Fe@P-PFP-Dox

The morphological structure of Fa-Fe@P-PFP-Dox was investigated by scanning electron microscopy (SEM, JEOL JSM-7800F) and transmission electron microscopy (TEM, Hitachi H-7600, Japan). The images of all samples were

captured. The average diameter of Fa-Fe@P-PFP-Dox was measured by a dynamic light scattering instrument (Nano, ZS90, Malvern instrument Ltd., UK). To study the optical property, the UV-vis absorption spectra of Fa-Fe@P-PFP-Dox, Fa@P-PFP-Dox, Fa@P-PFP, and Dox were recorded. After solvent extraction, the loading efficiency of Fe₃O₄ in Fa-Fe@P-PFP-Dox was determined by ICP-MS.

In vitro ADV Capability and Drug Release Behavior of Fa-Fe@P-PFP-Dox

The Fa-Fe@P-PFP-Dox suspension was irradiated by LIFU for different durations (pre, 1 min, 3 min, 5 min). The LIFU parameter was set as follows: power intensity 3.0 W/cm², 50% duty cycle, frequency 650 kHz. The corresponding optical microscopy images were captured, and ultrasound imaging of Fa-Fe@P-PFP-Dox was operated on an ultrasound imaging system. To detect the ADV-triggered drug release in vitro, Fa-Fe@P-PFP-Dox or Fa-Fe@P-Dox suspended in phosphate buffer (PBS) was irradiated by LIFU (3.0 W/cm²) for 5 min. Then, 3 mL of the treated suspensions were then placed in a dialysis bag with agitation. At each predetermined time point, 1 mL of aliquot was withdrawn for UV-vis examination. To assess Dox content, the absorbance at 480 nm of each sample was recorded and analyzed. The Fa-Fe@P-PFP-Dox without LIFU irradiation was set as the control group.

Cell Culture and HNE1 NPC Tumor-Bearing Mice Models

The HNE1 cell line was purchased from Shanghai Zhongqiao Xinzhou Biotechnology Co., Ltd (Shanghai, China), and cultured in RPMI-1640 medium (Invitrogen) with 10% serum and 1% penicillin-streptomycin solution at 37°C. Cells in the logarithmic phase were collected for the following experiments. BALB/c nude mice were purchased from Hunan STA Laboratory Animal Co., Ltd. All animal experiments were performed according to guidelines approved by the Medical Ethics Committee of Hainan General Hospital (Ethical approval No.: Med-Eth-Re-[2022]281). All procedures were complied with the “Guiding Principles in the Care and Use of Animals” (China) and the “Regulations for the Administration of Affairs Concerning Experimental Animals” (China). To establish NPC tumor-bearing mice models, HNE1 cells suspended in PBS (1 × 10⁶ cells, 100 μL) were subcutaneously injected into the flank of the mice.

Intracellular Uptake and in vitro Chemotherapy of Fa-Fe@P-PFP-Dox

To evaluate the cellular uptake of Fa-Fe@P-PFP-Dox, pre-seeded cells were incubated with Fa-Fe@P-PFP-Dox or Fe@P-PFP-Dox for different durations (1 h, 2 h, and 4 h), and fixed with 4% paraformaldehyde for 15 min. The cells were stained with DAPI, followed by observation under confocal laser scanning microscopy (CLSM). Besides, the intracellular uptake was also assessed by flow cytometry by measuring the fluorescence intensity of cells. In brief, cells cultured in 6-well plates were incubated with Fa-Fe@P-PFP-Dox or Fe@P-PFP-Dox for different durations (1 h, 2 h, and 4 h). Subsequently, cells were washed with PBS three times and digested with trypsin. The fluorescence intensities of cells were detected by flow cytometry.

To test the in vitro chemotherapeutic efficacy of Fa-Fe@P-PFP-Dox, HNE1 cells were cultured in 96-well plates for 24 h. Afterward, the cells were subjected to different treatments including (I) Control; (II) LIFU; (III) Fa-Fe@P-PFP-Dox; (IV) Fa-Fe@P-Dox + LIFU; (V) Fe@P-PFP-Dox + LIFU; (VI) Fa-Fe@P-PFP-Dox + LIFU. For the last three groups, cells were incubated with different nanoparticles for 4 h, received LIFU irradiation (3.0 W/cm², 5 min), and cultured for another 12 h. Finally, the relative cell viabilities were determined by a standard CCK-8 assay.

The Biodistribution and PA/MR Dual Imaging of Fa-Fe@P-PFP-Dox

To detect the in vivo biodistribution of Fa-Fe@P-PFP-Dox, mice bearing NPC were intravenously administrated with 200 μL of DiR-labeled Fe@P-PFP-Dox or Fa-Fe@P-PFP-Dox (the corresponding PLGA concentration was 10 mg/mL). Then the fluorescence images were recorded at 1, 2, 4, 6, and 24 h post-injection. Besides, at 2 h post-injection, the tumor tissues and major organs were collected for ex vivo imaging. The corresponding fluorescence intensities were analyzed.

To evaluate the PA imaging capability of Fa-Fe@P-PFP-Dox, Fe@P-PFP-Dox suspension at varying concentrations (1 mg/mL, 2 mg/mL, 3 mg/mL, 4 mg/mL, and 5 mg/mL) was irradiated by a PA laser and corresponding PA image were acquired using Vevo LAZR PA imaging system (Visual Sonics Inc., Toronto, Canada). Finally, the PA signal intensity of each image was measured by Vevo LAZR software. For the in vivo PA imaging, HNE1 tumor-bearing mice were

intravenously injected with 200 μ L of Fe@P-PFP-Dox or Fa-Fe@P-PFP-Dox (the corresponding PLGA concentration was 10 mg/mL). Then, PA images within the tumor region were recorded at 1, 2, 3, 4, 6, and 24 h post-injection. Furthermore, the PA signals were quantitatively measured.

To evaluate the MR imaging performance of Fa-Fe@P-PFP-Dox, the as-prepared Fa-Fe@P-PFP-Dox at the different Fe concentrations (0, 0.06, 0.13, 0.25, 0.5, and 1 mM) were placed in 1.5 mL EB tubes and serials T2-weighted MR scans were acquired using a clinical MR imaging system (Siemens Magnetom Skyra 3.0 T, Germany). Besides, HNE1 tumor-bearing mice were used for in vivo MR imaging. After intravenous injection of Fe@P-PFP-Dox or Fa-Fe@P-PFP-Dox, the T2-weighted MR images were acquired at 1, 2, 4, 6, and 24 h post-injection, and the MR signals were analyzed. Pseudo-coloring was applied to MR images using Matlab Software (2016). The percentage of signal decrease (PSD) was calculated as follows.

$$\text{PSD} = (\text{Signal}_{\text{post}} - \text{Signal}_{\text{pre}}) / \text{Signal}_{\text{pre}} \times 100\%$$

LIFU-Augmented Dox Distribution in Tumors

HNE1 tumor-bearing mice were intravenously injected with Fa-Fe@P-PFP-Dox (the corresponding PLGA concentration was 10 mg/mL). After 2 h of the injection, half of the mice were treated with LIFU irradiation (3.0 W/cm², 5 min). After that, all mice were sacrificed and tumor tissues were harvested for the frozen section to observe the biodistribution of Fa-Fe@P-PFP-Dox in tumors. The vessels were labeled by FITC-anti-CD31. To analyze the Dox accumulation in tumors, the tumor tissues were homogenized in 500 μ L of lysis buffer. Then tissue lysate was mixed with Triton-100. After vortexing, 1 mL of the extraction solution was added to the above tissue lysate and the samples were stored at -20°C for 18 hours. After centrifugation for 15 min, the fluorescence of the supernatant was assessed.

In vivo Chemotherapy of Fa-Fe@P-PFP-Dox

HNE1 tumor-bearing mice were randomly divided into six group (n = 5) including: (I) Control; (II) LIFU; (III) Fa-Fe@P-PFP-Dox; (IV) Fa-Fe@P-Dox + LIFU; (V) Fe@P-PFP-Dox + LIFU; (VI) Fa-Fe@P-PFP-Dox + LIFU. Two hours after the administration, LIFU at 3.0 W/cm² was employed to irradiate the tumor regions. The same process was repeated every two days. The body weight and tumor volumes were recorded during the therapeutic periods. At the end of treatment, the tumor tissues in each group were dissected for weight measurement and hematoxylin & eosin (H&E), proliferating cell nuclear antigen (PCNA), and terminal-deoxynucleotidyl transferase-mediated nick end labeling (TUNEL) staining. Besides, the major organs (heart, liver, spleen, lung, and kidney) were collected for H&E staining. The apoptotic index and proliferation index after treatments were analyzed.

Statistical Analysis

All values were presented as mean values \pm SD. The statistical analyses were carried out using the SPSS software (version 26.0), and the statistical analyses were conducted via a Student's *t*-test. Values with $P < 0.05$ are considered significant (* $p < 0.05$, ** $p < 0.01$, *** $p < 0.001$).

Results and Discussion

Synthesis and Characterization of Fa-Fe@P-PFP-Dox

In this study, Fa-modified and drug-loaded acoustic nanodroplets, Fa-Fe@P-PFP-Dox, were fabricated by a double-emulsion method (Figure 2A).⁴³ Such Fa-Fe@P-PFP-Dox were shown to be featured with uniform spherical structure, as evidenced by SEM (Figure 2B). Under TEM (Figure 2C), it was found that Fe₃O₄ particles were dispersed on the PLGA shell presented by the more evident darker contrast, indicating the efficient loading of Fe₃O₄. Besides, the successful encapsulation of Dox makes the Fa-Fe@P-PFP-Dox suspension red in color and all composites showed good dispersibility in aqueous solutions (Figure 2D). The dispersibility is desirable for the following in vitro and in vivo applications. As detected by dynamic light scattering (DLS), the hydrodynamic diameter of Fa-Fe@P-PFP-Dox was 215.7 ± 62.86 nm (Figure 2E). By recording the UV-vis spectrum of Dox, a characteristic absorption peak at 480 nm can be observed

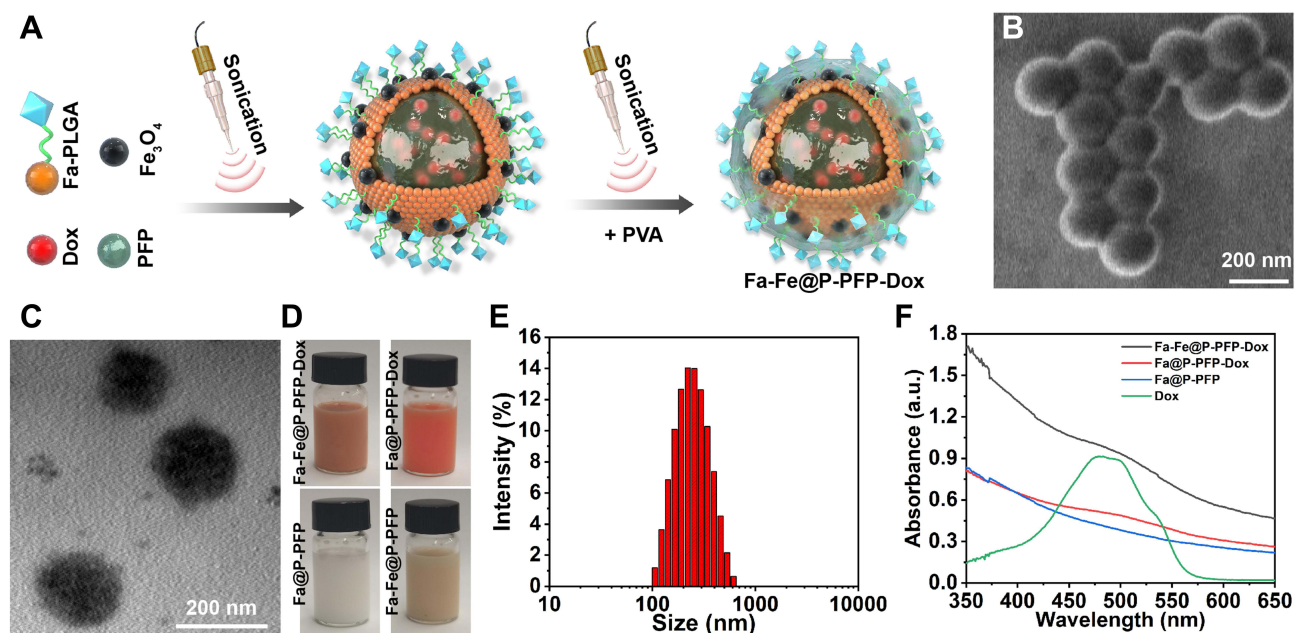


Figure 2 (A) Schematic illustration of the synthetic procedure of Fa-Fe@P-PFP-Dox nanodroplets. (B) SEM image and (C) TEM image of Fa-Fe@P-PFP-Dox nanodroplets. (D) Photographs of Fa-Fe@P-PFP-Dox, Fa@P-PFP-Dox, Fa@P-PFP and Fa-Fe@P-PFP. (E) The average diameter of Fa-Fe@P-PFP-Dox as detected by DLS. (F) UV-vis absorption spectra of Fa-Fe@P-PFP-Dox, Fa@P-PFP-Dox, Fa@P-PFP and Dox.

(Figure 2F). Meanwhile, the spectrum of Fa-Fe@P-PFP-Dox showed a similar peak at 480 nm, suggesting the successful encapsulation of Dox. However, there were no characteristic absorption bands detected with Fa@P-PFP. The loading efficacy of Dox in Fa-Fe@P-PFP-Dox was calculated to be 25.6%. By utilizing the coupled plasma mass spectrometry (ICP-MS), the loading efficacy of Fe_3O_4 was quantified to be 90.7%.

In vitro ADV Capability and Dox Release of Fa-Fe@P-PFP-Dox

It is reported that perfluorocarbon (PFC) could generate liquid-gas phase transition upon laser or acoustic stimulation, which can enable a controlled release.^{44,45} Some studies have developed PFC-based nanodroplets for US imaging because of their smaller size and higher stability than traditional microbubbles.^{26,28} Assisted by US irradiation, nano-sized droplets transfer to microbubbles, namely, the ADV effect.^{26,28} To investigate the liquid-gas phase transition effect, the Fa-Fe@P-PFP-Dox were irradiated by LIFU at different times and visualized under optical microscopy. At 1 min post-irradiation, no obvious microbubbles were observed, while a large number of microbubbles occurred at 3 min (Figure 3A). After continuous irradiation for 5 min, almost all Fa-Fe@P-PFP-Dox nanodroplets were converted into microbubbles. These results showed that the number of microbubbles increased with US irradiation time. Similar to the nanodroplet-to-microbubble phase transformation tendency, the in vitro US imaging performance of Fa-Fe@P-PFP-Dox was closely related to the LIFU irradiation time. Minimal echo enhancement was observed after 1 min of irradiation, while marked enhancement was detected after irradiation for 3–5 min (Figure 3B), which was consistent with the time-dependent bubble generation. The corresponding echo intensities were measured by US analysis software, which was in accordance with US images (Figure 3C). Therefore, the PFP in the core of Fa-Fe@P-PFP-Dox demonstrated an outstanding LIFU response and enhanced US imaging, providing the foundation for the following application.

Accompanied by increased size, the generated bubbles collapsed and the Dox in Fa-Fe@P-PFP-Dox would be released during ADV. Hence, the Dox releasing rate at different time points was determined. The Fa-Fe@P-PFP-Dox was irradiated by LIFU for 10 min at a power intensity of 3.0 W/cm^2 . As shown in Figure 3D, more than 50% of Dox in Fa-Fe@P-PFP-Dox was released at 6 h and the release rate tended to flat out over 24 h. However, in the absence of LIFU irradiation, only 37.03% of Dox was released within 48 h. Even with US irradiation, Fa-Fe@P-Dox without PFP encapsulation could not release a large amount of Dox within 48 h (46.19%). These results demonstrated that both LIFU

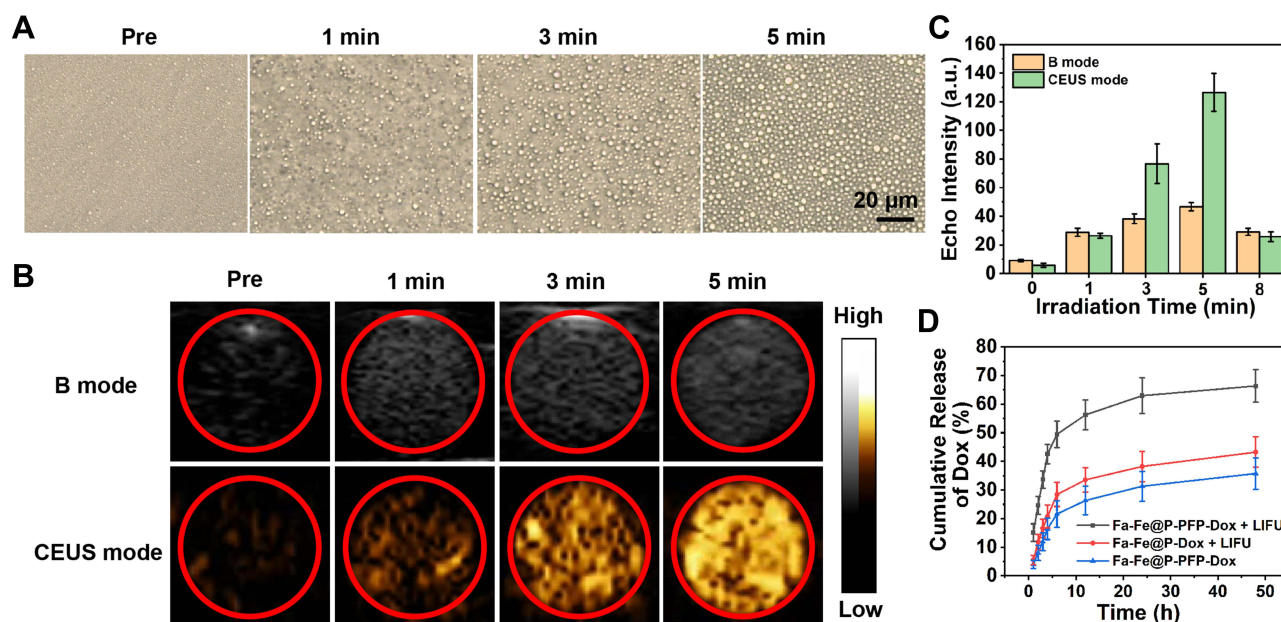


Figure 3 (A) Optical images of Fa-Fe@P-PFP-Dox before and after LIFU irradiation for different times (1 min, 3 min and 5 min). (B) US imaging of Fa-Fe@P-PFP-Dox in B mode and CEUS mode with prolonged LIFU irradiation time. (C) Echo intensities of FA-H@NDs in B mode and contrast mode. (D) Dox release curves of Fa-Fe@P-PFP-Dox with or without LIFU irradiation and Fa-Fe@P-Dox with LIFU irradiation.

irradiation and PFP encapsulation are important factors affecting the release of Dox. LIFU could act as an external stimulation to achieve the on-demand Dox release from Fa-Fe@P-PFP-Dox acoustic nanodroplets.

Cell Targeting Capability and in vitro Chemotherapy of Fa-Fe@P-PFP-Dox Against HNE1

Efficient cellular uptake of Fa-Fe@P-PFP-Dox is a prerequisite for exerting a therapeutic effect. To improve the tumor uptake of the as-synthesized acoustic nanodroplets, Fa, a targeting ligand, was conjugated to the surface of the nanocarriers for their recognition of folate receptors that was overexpressed in NPC. Hence, the Fa-mediated endocytosis was visualized by CLSM. As depicted in Figure 4A, without the guidance of Fa, minimal Fe@P-PFP-Dox accumulated into the HNE1 cells, while Fa-Fe@P-PFP-Dox was taken up efficiently by HNE1 cells, and phagocytosis was enhanced with prolonged incubation time. The fluorescence intensity of cells measured by flow cytometry in Fa-Fe@P-PFP-Dox-treated cells was higher than that of Fe@P-PFP-Dox-treated cells (Figure 4B and C), which is similar to CLSM observations, demonstrating that Fa favored the accumulation of Dox-loaded nanodroplets in HNE1 cells.

As a powerful nano-delivery system, Fa-Fe@P-PFP-Dox acoustic nanodroplets offer significant potential for cancer chemotherapy. Having demonstrated the intracellular uptake of Fa-Fe@P-PFP-Dox by HNE1 cells, in vitro therapeutic efficacy was assessed by the CCK-8 assay next. As is shown in Figure 4D, the majority of cells remained alive after LIFU irradiation. In the presence of Dox, the cells suffered from serious damage. In detail, the cell viabilities in the Fa-Fe@P-PFP-Dox group and Fa-Fe@P-Dox + LIFU were $76.66 \pm 10.34\%$ and $68.24 \pm 8.94\%$ respectively. Upon LIFU irradiation, PFP-loaded nanocarriers underwent ADV and released Dox, which enhanced the chemotherapy with the cell viability of $51.34 \pm 6.02\%$ in the Fe@P-PFP-Dox + LIFU treatment group, and the therapeutic efficacy was further enhanced by Fa modification (Fa-Fe@P-PFP-Dox + LIFU, $30.84 \pm 6.95\%$).

The Biodistribution and PA/MR Dual Imaging of Fa-Fe@P-PFP-Dox

To further assess the targeting ability of Fa-Fe@P-PFP-Dox in vivo, fluorescence imaging of nude mice bearing HNE1 xenografts was performed after intravenous injection of Fa-Fe@P-PFP-Dox or Fe@P-PFP-Dox labeled with DiR. As shown in Figure 5A and B, fluorescence signals in tumor regions rapidly increased at 1 h after intravenous injection of

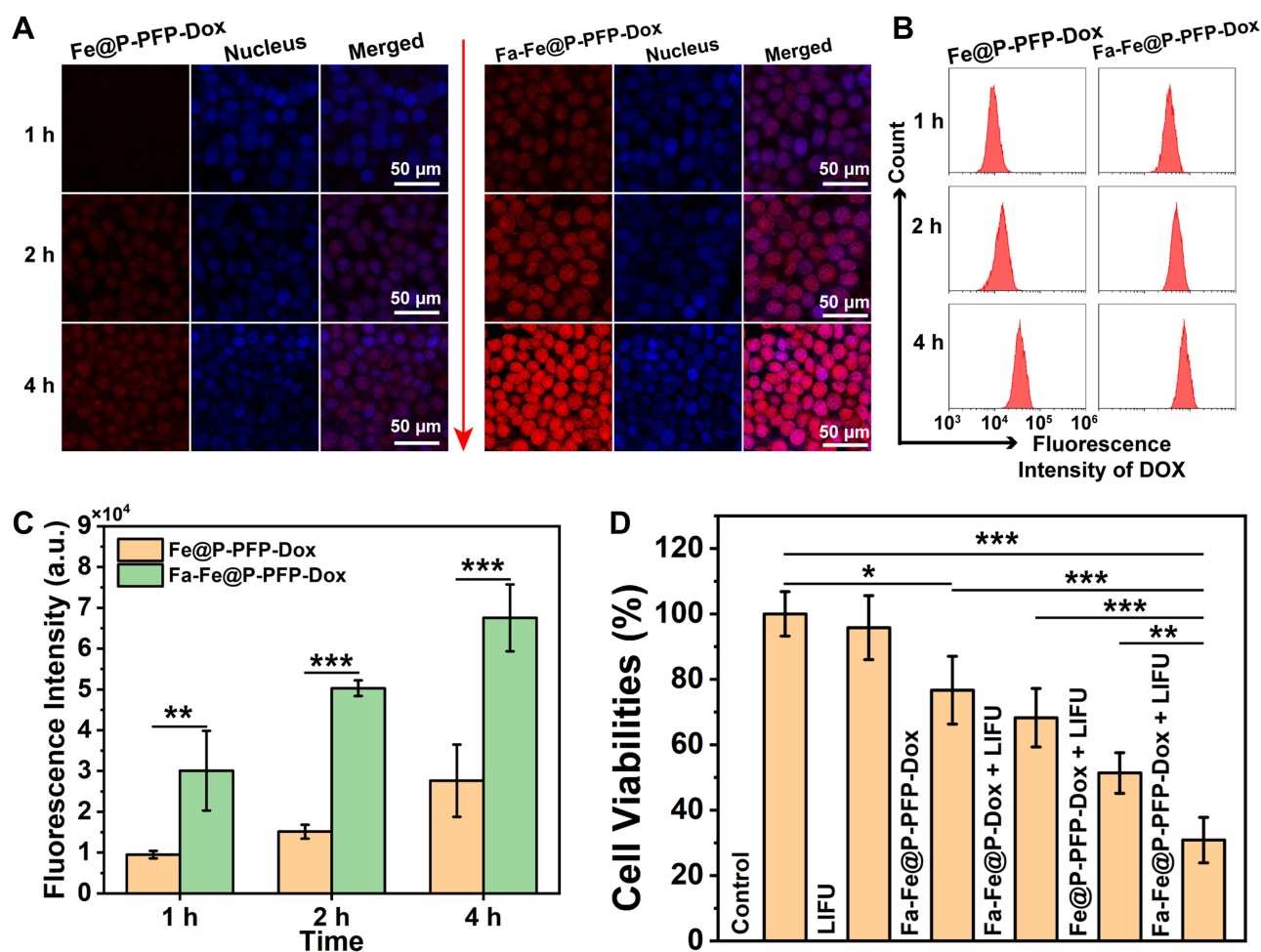


Figure 4 (A) Intracellular uptake of Fa-Fe@P-PFP-Dox and Fe@P-PFP-Dox by HNE1 cells was detected by CLSM after different incubation times (1 h, 2 h, and 4 h). (B and C) Flow cytometry analysis of intracellular uptake of FA-H@NDs and H@NDs. (D) Relative cell viabilities of HNE1 cells after various treatments. The statistical analyses were conducted via a Student's *t*-test, **p* < 0.05, ***p* < 0.01, ****p* < 0.001.

Fa-Fe@P-PFP-Dox, reached the peak at 2 h, and then gradually decreased. Fluorescence signals could still be detected 24 h after injection, indicating the long circulation time of Fa-Fe@P-PFP-Dox, which would be beneficial for Dox-based chemotherapy. In contrast, negligible fluorescence signals were observed in tumors after injection of Fe@P-PFP-Dox, which may be due to the lack of Fa guidance. This conclusion was further verified by ex vivo fluorescence imaging of tumor tissues and major organs collected from mice (Figure 5C). The fluorescence signal of tumor tissue in the Fa-Fe@P-PFP-Dox group was stronger than that of the Fe@P-PFP-Dox group (Figure 5D), which further demonstrated that the modification with Fa greatly improved the tumor-targeting efficiency of such nanocarriers.

Precision medicine has made great progress in recent years, especially in the application of imaging-guided cancer therapy.^{33,46} Multimodal imaging could be used during the therapeutic process to trace the distribution of chemotherapeutic drugs,⁴⁷ according to which the time window of external LIFU irradiation could be determined more accurately. On account of the PA properties of Fe₃O₄, Fe₃O₄-loaded nanoparticles were anticipated to be an excellent PA imaging contrast agent. Here, the PA imaging performance of Fa-Fe@P-PFP-Dox both in vitro and in HNE1 tumor-bearing mice was analyzed by a PA imaging system. As shown in Figure 6A, the PA intensity of Fa-Fe@P-PFP-Dox displayed a concentration-dependent enhancement with a good linear correlation. Meanwhile, tumor-bearing mice were intravenously administrated with Fa-Fe@P-PFP-Dox or Fe@P-PFP-Dox and the PA intensities of the tumors were compared. Consistent with the fluorescence imaging, there was the highest PA signal at 2 h post-Fa-Fe@P-PFP-Dox injection, and gradually decreased with blood circulation time (Figure 6B and C). As for the mice that received Fe@P-PFP-Dox

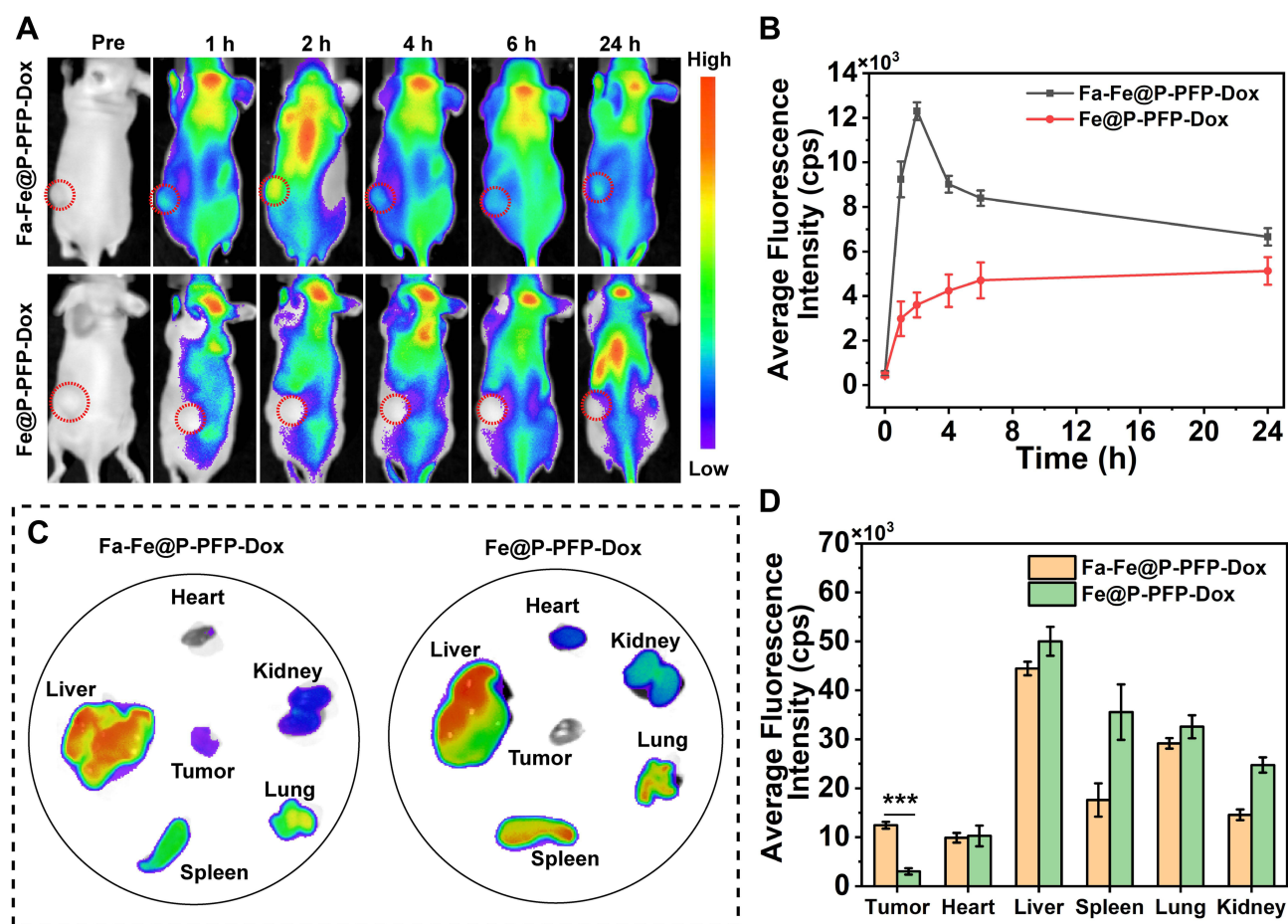


Figure 5 (A) In vivo fluorescence imaging at different time points after intravenous injection of DiR-labeled Fa-Fe@P-PFP-Dox and Fe@P-PFP-Dox in HNE1 tumor-bearing mice. (B) the corresponding tumor fluorescence intensities over time. (C) Ex vivo fluorescence imaging pictures and (D) corresponding quantitative analysis of fluorescence intensity of tumor tissues and major organs dissected from the above mice 2 hours after injection. The statistical analyses were conducted via a Student's *t*-test, ****p* < 0.001.

administration, the PA signal in the tumor region only increased slightly as a result of the limited aggregation of Fe@P-PFP-Dox. In view of the above results, Fa-Fe@P-PFP-Dox has proved to be a desired contrast agent to enhance PA imaging under the guidance of folate targeting.

In addition to acting as a PA contrast agent, Fe₃O₄ has been used to enhance T₂-weighted MR imaging.^{41,42} Fa-Fe@P-PFP-Dox is expected to be desirable for contrast-enhanced T₂-weighted MR imaging, which was further systematically evaluated both in vitro and in vivo. It was found that the brightness of corresponding MR images declined with Fa-Fe@P-PFP-Dox concentration, presenting a well-correlated linear relationship between 1/T₂ values and Fe concentration, based on which the r² value of the Fa-Fe@P-PFP-Dox was calculated to be 60.14 mM⁻¹ s⁻¹ (Figure 7A). The transverse relaxation time was greatly shortened by the Fa-Fe@P-PFP-Dox, indicating the outstanding contrast-enhanced performance of Fa-Fe@P-PFP-Dox for T₂-weighted MR. Based on the in vitro MR imaging performance of Fa-Fe@P-PFP-Dox, the in vivo MR imaging was further carried out. As shown in Figure 7B and C, the PSD significantly increased to 74.95 ± 5.30% at 2 h after intravenous injection of Fa-Fe@P-PFP-Dox and gradually declined to 53.46 ± 2.77% within 24 h, suggesting the effective accumulation of Fa-Fe@P-PFP-Dox in the tumor tissues. However, the PSD only increased by less than 40% in the mice injected with Fe@P-PFP-Dox. It is concluded that Fa-Fe@P-PFP-Dox was endowed with favorable PA and MR dual imaging capability. The incorporation of the image-guidance capability to the external LIFU-triggered-response further potentially pushed the development of precision medicine forward.

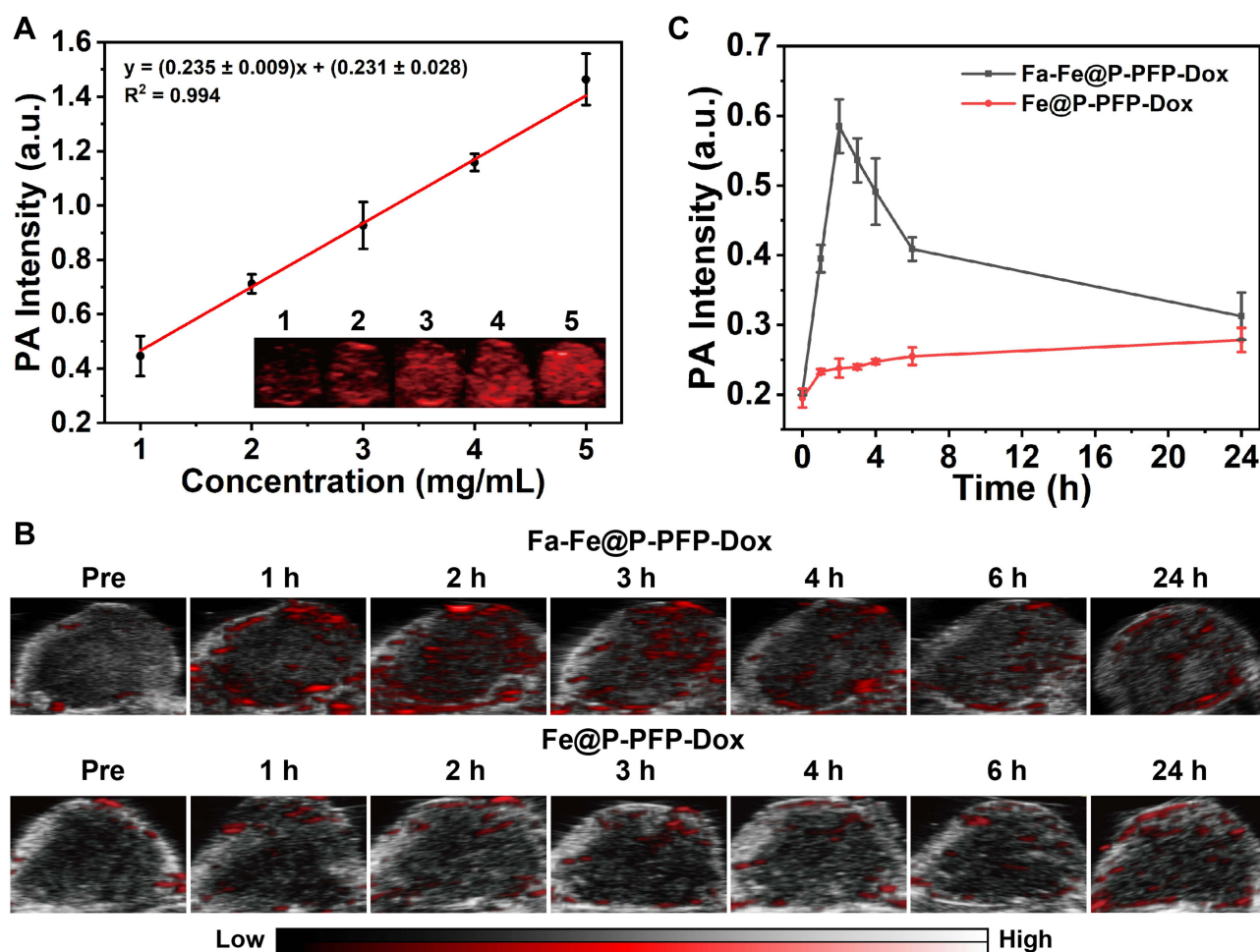


Figure 6 (A) In vitro PA images and corresponding PA intensities of Fa-Fe@P-PFP-Dox at different concentrations. (B) In vivo PA imaging and (C) corresponding PA intensities over time after intravenous injection of Fa-Fe@P-PFP-Dox.

LIFU-Augmented Dox Distribution in Tumors

When therapeutic drugs reach the tumor mass, they usually distribute near the vasculatures and hardly penetrate into inner tissue due to the pathophysiological characteristics of tumors, resulting in unsatisfactory drug distribution, which seriously hinders the anticancer efficacy.^{48,49} We attempted to improve the effective intratumoral diffusion of chemotherapeutic drugs through the LIFU-triggered ADV effect in this study. Upon LIFU irradiation, the PFP can produce effective ADV followed by tissue erosion, which is favorable to drug infiltration. The distribution of Dox in the tumor tissues was investigated by comparing the red fluorescence of Dox with or without LIFU irradiation (ie, with or without ADV). As depicted in Figure 8A, tumor vasculatures were stained by FITC- anti-CD31 (green fluorescence) and Dox presented red fluorescence. Dox in the control group without LIFU irradiation only gathered near blood vessels. Comparatively, after LIFU irradiation, Dox not only diffused around blood vessels but also penetrate into tumors farther away from blood vessels. In addition, observation on Dox distribution in tumor tissue was conducted by frozen section. In the case of the ADV group, significant red fluorescence was evenly distributed in tumor tissue, while only weak fluorescence can be detected in the group without ADV (Figure 8B). The result illustrated that the LIFU-triggered ADV effect is essential to promoting drug permeation. The Dox content in tumors was measured, and there was a significant difference between the two groups with or without LIFU irradiation (Figure 8C). For the LIFU-triggered ADV group, the Dox content was $3.49 \pm 0.20 \mu\text{g/g}$ (Dox/tumor), higher than that of the control group ($2.55 \pm 0.23 \mu\text{g/g}$). The result should be ascribed to the following four aspects: (1) LIFU-triggered ADV effect disrupts tumor vascular endothelial gap, facilitating more nanocarriers in blood circulation to enter into tumor tissues. (2) LIFU-triggered ADV effect could achieve the “on-demand” release of the loaded Dox at the tumor

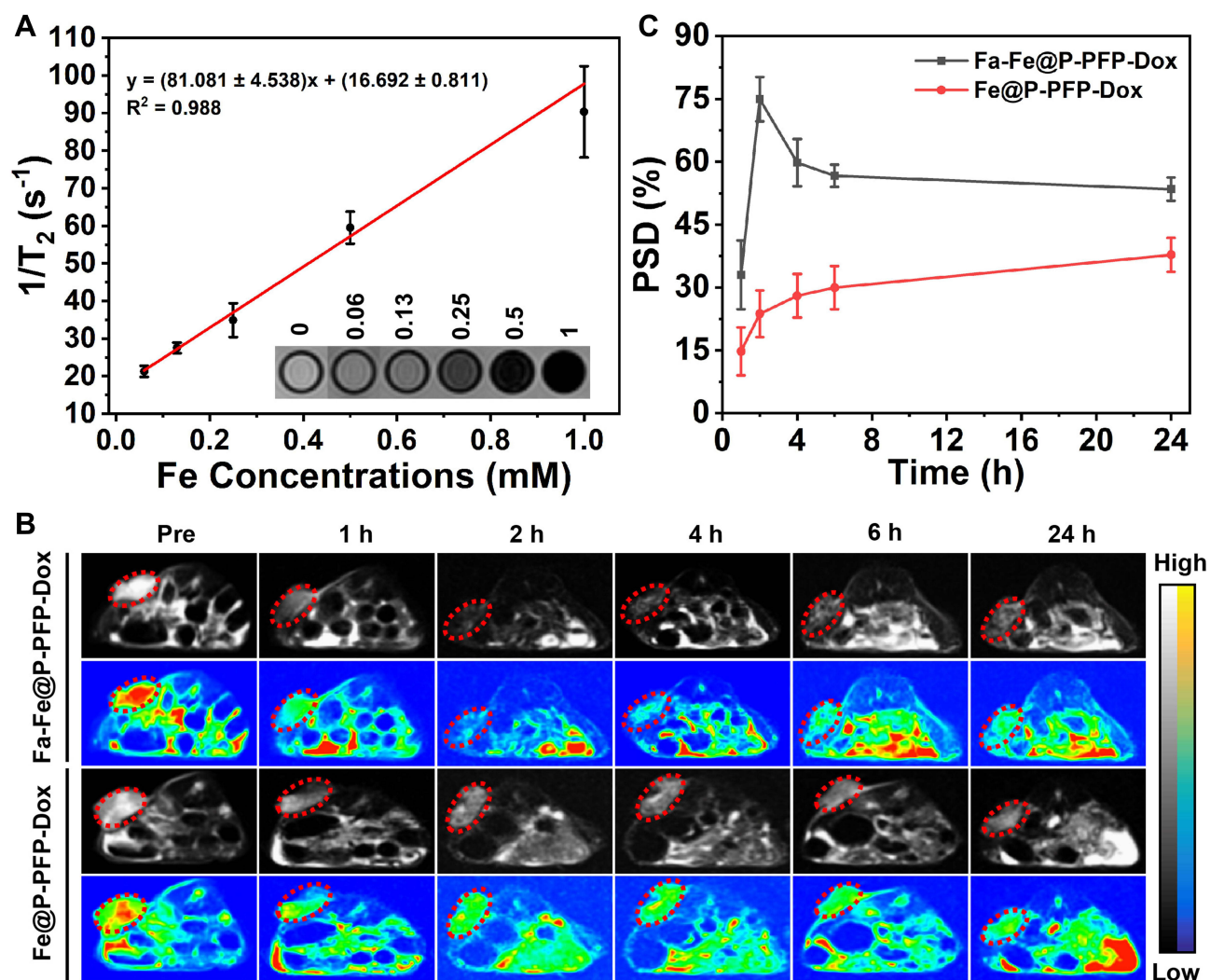


Figure 7 (A) The curve of $1/T_2$ versus Fe concentration under T_2 -weighted MR imaging. Inset: T_2 -weighted MR imaging of Fa-Fe@P-PFP-Dox at different Fe concentrations. (B) MR images (top: grayscale images; bottom: pseudo-coloring images) of HNE1 tumors (region enveloped by red dotted line) before and after intravenous injection of Fa-Fe@P-PFP-Dox and Fe@P-PFP-Dox. (C) Quantitative analysis of decreased MR signal intensities over time.

sites, which has also been demonstrated in this study. (3) Compared with Dox-loaded overlarge size nanocarriers, the size of released Dox is much smaller, and naturally smaller size drugs could easily penetrate into deep tumor parenchyma. (4) Blast effect induced by nanodroplets combined with LIFU irradiation may destroy the barriers, allowing the drug to penetrate away from the blood vessels.

In vivo Chemotherapy of Fa-Fe@P-PFP-Dox

Based on the aforementioned evaluation and discussion, the potential in vivo LIFU-triggered chemotherapy was investigated. To this end, HNE1 tumor-bearing mice were assigned to the following groups: (I) Control; (II) LIFU; (III) Fa-Fe@P-PFP-Dox; (IV) Fa-Fe@PFP-Dox + LIFU; (V) Fe@P-PFP-Dox + LIFU; (VI) Fa-Fe@P-PFP-Dox + LIFU. According to the in vivo distribution (in vivo fluorescence imaging), PA, and MR imaging data, a large number of FA-H@NDs were enriched in tumors 2 h after injection. Therefore, LIFU irradiation was employed 2 h after injection to promote Dox release and deep tumor penetration. Treatments were performed every three days and the detailed experimental scheme is displayed in Figure 9A. Tumour volumes and body weights were measured during the treatments. According to tumor growth curves and digital photographs (Figure 9B and C), compared to the control group, the tumors in the LIFU-treated group grew rapidly, exhibiting little therapeutic effect. The tumor growth in the Fa-Fe@P-PFP-Dox

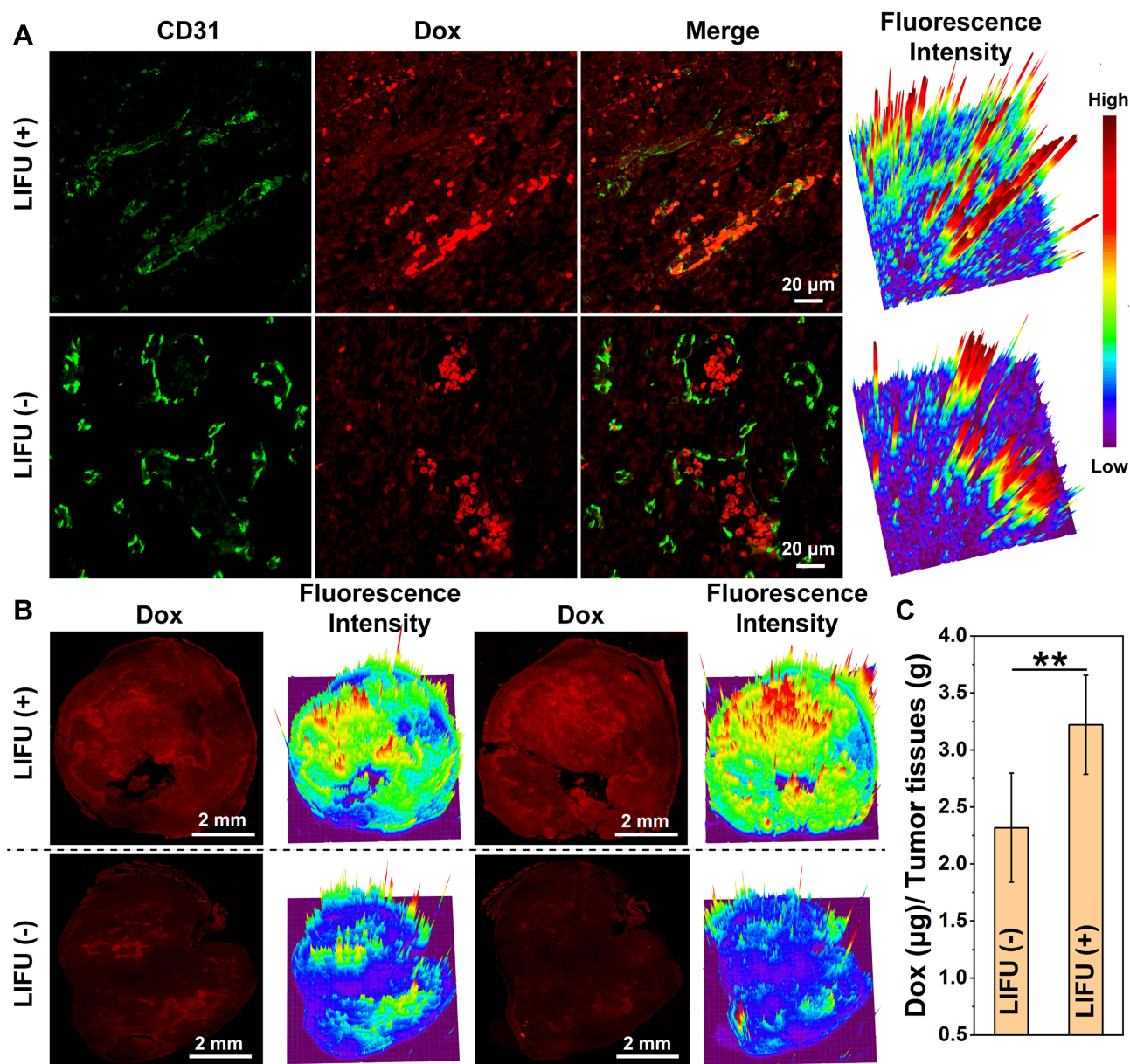


Figure 8 (A) Extravascular distribution of Dox (red fluorescence) with or without LIFU irradiation. Blood vasculature was stained in green. **(B)** Fa-Fe@P-PFP-Dox distribution in different tumor sections with or without LIFU irradiation. **(C)** Dox contents in tumors with or without LIFU irradiation. The statistical analyses were conducted via a Student's *t*-test, ***p* < 0.01.

and Fa-Fe@P-Dox+LIFU groups was inhibited to a certain extent, but the tumors still maintained rapid growth. Fe@P-PFP-Dox + LIFU and Fa-Fe@P-PFP-Dox + LIFU showed obvious inhibitory effects on tumor growth, indicating that Dox was effectively released after LIFU irradiation, thereby killing tumor cells. Tumor mass and tumor volume showed the same trend (Figure 9D). Comparatively, Fa-Fe@P-PFP-Dox + LIFU exhibited the highest tumor inhibition rate ($74.24 \pm 7.95\%$) among all groups (Figure 9E). During the therapeutic period, there was no significant fluctuation in body weight (Figure 9F), indicating the high therapeutic biosafety of these drug-loaded acoustic nanodroplets.

At the end of treatments, HE staining was conducted to visualize the morphologic change of tumor cells (Figure 10A). The results showed that the tumor cells in control and LIFU groups were closely arranged, with normal cell morphology or status. However, different degrees of cell damage (eg, karyopyknosis, karyorrhexis, and karyolysis) occurred in the other Dox-contained groups. The TUNEL staining was performed to detect apoptosis (green fluorescence) in tumors after various treatments (Figure 10A and B). It turns out that the cells in Fa-Fe@P-PFP-Dox + LIFU group exhibited the highest apoptosis

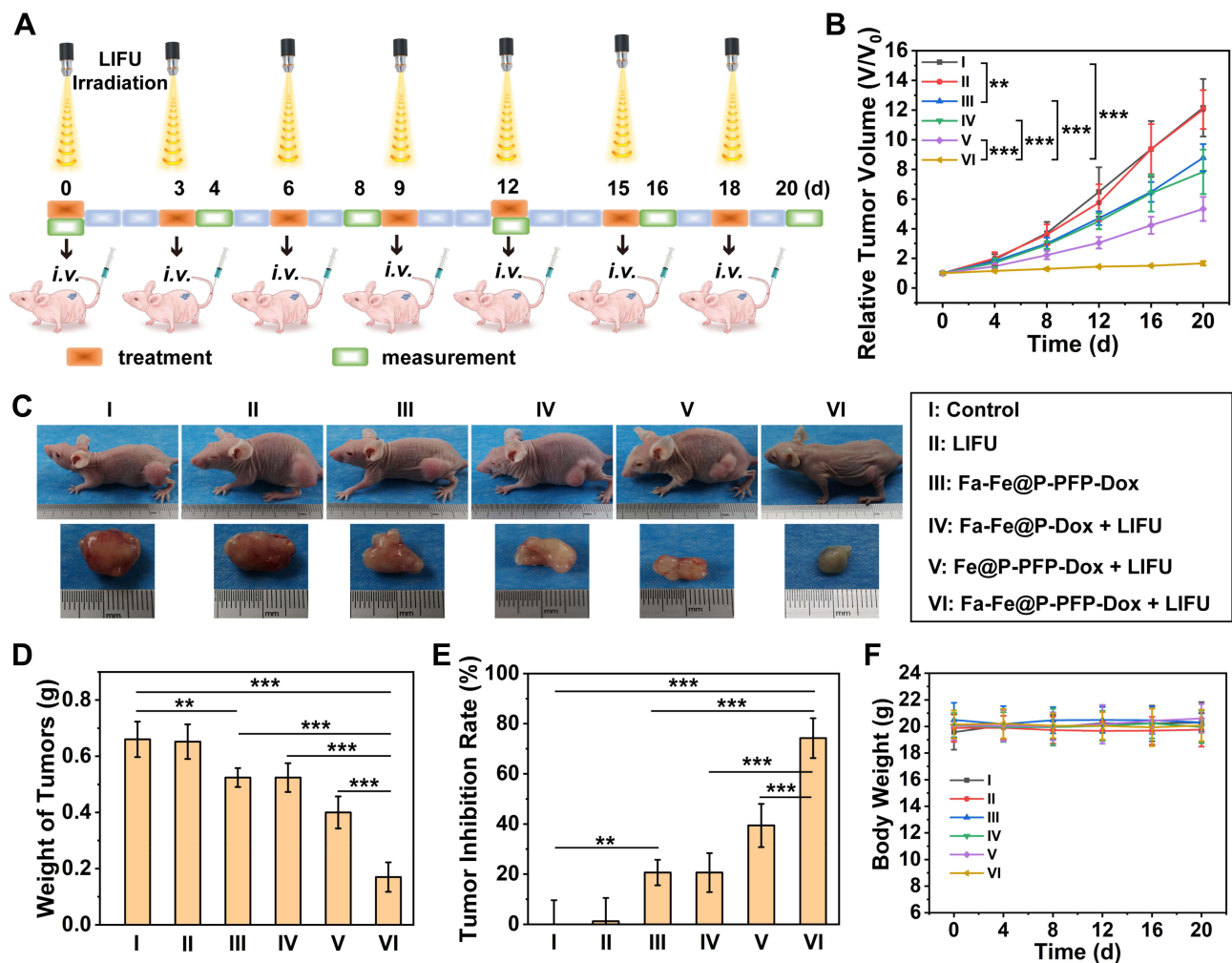


Figure 9 (A) In vivo therapeutic protocol of chemotherapy on HNE1 tumor-bearing mice. (B) Time-dependent relative tumor volumes post-treatment for different groups. (C) Digital photographs of tumor-bearing mice and the corresponding tumor masses at 20 days post different treatments. (D) Tumor weights post-treatment for different groups. (E) Tumor inhibition rates in each group according to the tumor weights. (F) Time-dependent body-weight curves of mice in each group. The statistical analyses were conducted via a Student's *t*-test, ***p* < 0.01, ****p* < 0.001.

index ($93.54 \pm 4.64\%$) compared with other groups. The PCNA staining displayed the same tendency as HE and TUNEL results, with the proliferation index ($8.30 \pm 4.85\%$) in the Fa-Fe@P-PFP-Dox + LIFU group significantly lower than in other groups (Figure 10A and C). Additionally, the major organs of mice were collected for HE staining (Figure 10D). It was found that no significant adverse effects on the organs during the treatment period, further indicating the high biosafety of this therapeutic modality. Based on these results, we conclude that the combination of Dox-loaded acoustic nanodroplets, Fa-Fe@P-PFP-Dox, with LIFU irradiation could exert a powerful therapeutic effect on NPC. Indeed, our study demonstrated desirable biosafety and excellent therapeutic effect of the nanodroplets, we are meticulously planning the next stage of work. We think our strategy needs to be consolidated in the following perspectives. To begin with, we will optimize our preparation method, so that the nanodroplets can be produced more efficiently, and also with a high standard of quality control. Meanwhile, we will explore a proper storage method to make sure the reagents can be preserved in the mid-to-long term without compromising their stability. Most importantly, more detailed biological safety assay will be explored. We will continuously improve our results based on the experimental feedback.

Conclusion

In summary, Fa-modified and drug-loaded acoustic nanodroplets have been successfully constructed for dual-imaging guided highly efficient chemotherapy against NPC. Upon intravenous administration, these acoustic nanodroplets

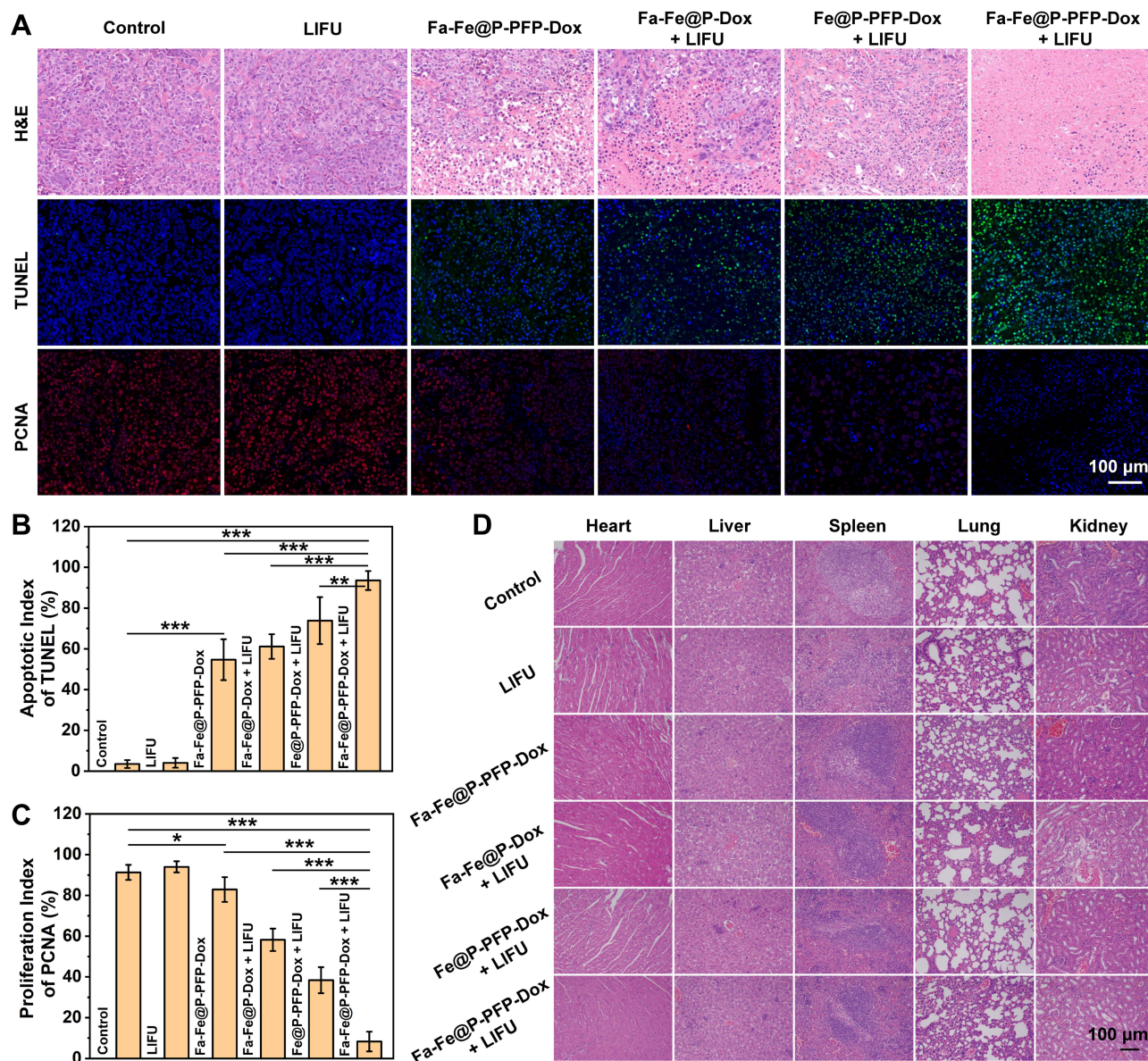


Figure 10 (A) H&E staining, TUNEL staining, and PCNA immunofluorescence staining in tumor sections from each experimental group. (B and C) The corresponding apoptotic index and proliferative index post-treatment for different groups. (D) H&E staining of major organs post-treatment for different groups. The statistical analyses were conducted via a Student's *t*-test, **p* < 0.05, ***p* < 0.01, ****p* < 0.001.

exhibit enhanced intracellular uptake and tumor accumulation, which was visualized by PA/MR dual-modal imaging. In the presence of LIFU irradiation at the tumor site, the accumulated nano-sized droplets would readily transfer into microbubbles via the ADV effect. The droplets would continuously inflate until collapse, achieving an on-demand release of Dox. Besides, Dox penetration could also be improved following LIFU irradiation. As a result, Fa-Fe@P-PFP-Dox demonstrates significant therapeutic efficacy against NPC. Our study demonstrates that Fa-modified acoustic nanodroplets can be an innovative drug carrier with a significantly improved anticancer efficacy against NPC.

Acknowledgments

This work was supported by the National Natural Science Foundation of China (Grant Nos. 81871365, 81760317, and 82160337) and the Hainan Province Science and Technology Special Fund (Grant Nos. ZDYF2019136, ZDYF2020138, and ZDYF2020140).

Disclosure

The authors report no conflicts of interest in this work.

References

1. Chen YP, Chan ATC, Le QT, Blanchard P, Sun Y, Ma J. Nasopharyngeal carcinoma. *Lancet*. 2019;394(10192):64–80. doi:10.1016/s0140-6736(19)30956-0
2. Lee AW, Ma BB, Ng WT, Chan AT. Management of nasopharyngeal carcinoma: current practice and future perspective. *J Clin Oncol*. 2015;33(29):3356–3364. doi:10.1200/jco.2015.60.9347
3. Chen YP, Ismaila N, Chua MLK, et al. Chemotherapy in combination with radiotherapy for definitive-intent treatment of stage II-IVA nasopharyngeal carcinoma: CSCO and ASCO guideline. *J Clin Oncol*. 2021;39(7):840–859. doi:10.1200/jco.20.03237
4. You R, Liu YP, Huang PY, et al. Efficacy and safety of locoregional radiotherapy with chemotherapy vs chemotherapy alone in de novo metastatic nasopharyngeal carcinoma: a multicenter Phase 3 randomized clinical trial. *JAMA Oncol*. 2020;6(9):1345–1352. doi:10.1001/jamaoncol.2020.1808
5. Hong RL, Hsiao CF, Ting LL, et al. Final results of a randomized Phase III trial of induction chemotherapy followed by concurrent chemoradiotherapy versus concurrent chemoradiotherapy alone in patients with stage IVA and IVB nasopharyngeal carcinoma-Taiwan Cooperative Oncology Group (TCOG) 1303 Study. *Annals Oncol*. 2018;29(9):1972–1979. doi:10.1093/annonc/mdy249
6. Kerbel RS, Andre N. Adjuvant metronomic chemotherapy for locoregionally advanced nasopharyngeal carcinoma. *Lancet*. 2021;398(10297):278–279. doi:10.1016/s0140-6736(21)01240-x
7. Chen YP, Liu X, Zhou Q, et al. Metronomic capecitabine as adjuvant therapy in locoregionally advanced nasopharyngeal carcinoma: a multicentre, open-label, parallel-group, randomised, controlled, phase 3 trial. *Lancet*. 2021;398(10297):303–313. doi:10.1016/s0140-6736(21)01123-5
8. Danhier F, Feron O, Pr at V. To exploit the tumor microenvironment: passive and active tumor targeting of nanocarriers for anti-cancer drug delivery. *J Control Release*. 2010;148(2):135–146. doi:10.1016/j.jconrel.2010.08.027
9. Nishijima TF, Deal AM, Williams GR, Sanoff HK, Nyrop KA, Muss HB. Chemotherapy toxicity risk score for treatment decisions in older adults with advanced solid tumors. *Oncologist*. 2018;23(5):573–579. doi:10.1634/theoncologist.2017-0559
10. He C, Tang Z, Tian H, Chen X. Co-delivery of chemotherapeutics and proteins for synergistic therapy. *Adv Drug Deliv Rev*. 2016;98:64–76. doi:10.1016/j.addr.2015.10.021
11. Patra JK, Das G, Fraceto LF, et al. Nano based drug delivery systems: recent developments and future prospects. *J Nanobiotechnology*. 2018;16(1):71. doi:10.1186/s12951-018-0392-8
12. Nair M, Sandhu SS, Sharma AK. Cancer molecular markers: a guide to cancer detection and management. *Semin Cancer Biol*. 2018;52(Pt 1):39–55. doi:10.1016/j.semcancer.2018.02.002
13. Le Tourneau C, Delord JP, Goncalves A, et al. Molecularly targeted therapy based on tumour molecular profiling versus conventional therapy for advanced cancer (SHIVA): a multicentre, open-label, proof-of-concept, randomised, controlled Phase 2 trial. *Lancet Oncol*. 2015;16(13):1324–1334. doi:10.1016/s1470-2045(15)00188-6
14. Huang A, Garraway LA, Ashworth A, Weber B. Synthetic lethality as an engine for cancer drug target discovery. *Nat Rev Drug Discov*. 2020;19(1):23–38. doi:10.1038/s41573-019-0046-z
15. Scaranti M, Cojocaru E, Banerjee S, Banerji U. Exploiting the folate receptor α in oncology. *Nat Rev Clin Oncol*. 2020;17(6):349–359. doi:10.1038/s41571-020-0339-5
16. Assaraf YG, Leamon CP, Reddy JA. The folate receptor as a rational therapeutic target for personalized cancer treatment. *Drug Resist Updat*. 2014;17(4–6):89–95. doi:10.1016/j.drug.2014.10.002
17. Farran B, Montenegro RC, Kasa P, et al. Folate-conjugated nanovehicles: strategies for cancer therapy. *Mater Sci Eng C Mater Biol Appl*. 2020;107:110341. doi:10.1016/j.msec.2019.110341
18. Xie M, Zhang H, Xu Y, et al. Expression of folate receptors in nasopharyngeal and laryngeal carcinoma and folate receptor-mediated endocytosis by molecular targeted nanomedicine. *Int J Nanomedicine*. 2013;8:2443–2451. doi:10.2147/ijn.S46327
19. Alibolandi M, Abnous K, Sadeghi F, Hosseinkhani H, Ramezani M, Hadizadeh F. Folate receptor-targeted multimodal polymersomes for delivery of quantum dots and doxorubicin to breast adenocarcinoma: in vitro and in vivo evaluation. *Int J Pharm*. 2016;500(1–2):162–178. doi:10.1016/j.ijpharm.2016.01.040
20. Huang Y, Wang T, Tan Q, et al. Smart stimuli-responsive and mitochondria targeting delivery in cancer therapy. *Int J Nanomedicine*. 2021;16:4117–4146. doi:10.2147/ijn.S315368
21. Mitchell MJ, Billingsley MM, Haley RM, Wechsler ME, Peppas NA, Langer R. Engineering precision nanoparticles for drug delivery. *Nat Rev Drug Discov*. 2021;20(2):101–124. doi:10.1038/s41573-020-0090-8
22. Carson AR, McTiernan CF, Lavery L, et al. Ultrasound-targeted microbubble destruction to deliver siRNA cancer therapy. *Cancer Res*. 2012;72(23):6191–6199. doi:10.1158/0008-5472.Can-11-4079
23. Sun W, Li Z, Zhou X, Yang G, Yuan L. Efficient exosome delivery in refractory tissues assisted by ultrasound-targeted microbubble destruction. *Drug Deliv*. 2019;26(1):45–50. doi:10.1080/10717544.2018.1534898
24. Tang K, Zhang Y, Zhang H, et al. Delivery of chemotherapeutic drugs in tumour cell-derived microparticles. *Nat Commun*. 2012;3:1282. doi:10.1038/ncomms2282
25. Narang AS, Varia S. Role of tumor vascular architecture in drug delivery. *Adv Drug Deliv Rev*. 2011;63(8):640–658. doi:10.1016/j.addr.2011.04.002
26. Yang C, Zhang Y, Luo Y, et al. Dual ultrasound-activatable nanodroplets for highly-penetrative and efficient ovarian cancer theranostics. *J Mater Chem B*. 2020;8(3):380–390. doi:10.1039/c9tb02198a
27. Zhang L, Yi H, Song J, et al. Mitochondria-targeted and ultrasound-activated nanodroplets for enhanced deep-penetration sonodynamic cancer therapy. *ACS Appl Mater Interfaces*. 2019;11(9):9355–9366. doi:10.1021/acsami.8b21968
28. Ho YJ, Yeh CK. Theranostic performance of acoustic nanodroplet vaporization-generated bubbles in tumor intertissue. *Theranostics*. 2017;7(6):1477–1488. doi:10.7150/thno.19099

29. Zhu L, Zhao H, Zhou Z, et al. Peptide-functionalized phase-transformation nanoparticles for low intensity focused ultrasound-assisted tumor imaging and therapy. *Nano Lett.* 2018;18(3):1831–1841. doi:10.1021/acs.nanolett.7b05087
30. Sun Q, Zhou Z, Qiu N, Shen Y. Rational design of cancer nanomedicine: nanoproperty integration and synchronization. *Adv Mater.* 2017;29(14):1606628. doi:10.1002/adma.201606628
31. Kim SM, Faix PH, Schnitzer JE. Overcoming key biological barriers to cancer drug delivery and efficacy. *J Control Release.* 2017;267:15–30. doi:10.1016/j.jconrel.2017.09.016
32. Snipstad S, Vikedal K, Maardalen M, Kurbatskaya A, Sulheim E, Davies CL. Ultrasound and microbubbles to beat barriers in tumors: improving delivery of nanomedicine. *Adv Drug Deliv Rev.* 2021;177:113847. doi:10.1016/j.addr.2021.113847
33. Cai W, Fan G, Zhou H, et al. Self-assembled hybrid nanocomposites for multimodal imaging-guided photothermal therapy of lymph node metastasis. *ACS Appl Mater Interfaces.* 2020;12(44):49407–49415. doi:10.1021/acsami.0c14576
34. Siddique S, Chow JCL. Application of nanomaterials in biomedical imaging and cancer therapy. *Nanomater.* 2020;10(9):1700. doi:10.3390/nano10091700
35. Siddique S, Chow JCL. Gold nanoparticles for drug delivery and cancer therapy. *Appl Sci.* 2020;10(11):3824. doi:10.3390/app10113824
36. Barentsz J, Takahashi S, Oyen W, et al. Commonly used imaging techniques for diagnosis and staging. *J Clin Oncol.* 2006;24(20):3234–3244. doi:10.1200/jco.2006.06.5946
37. Chow JCL. Magnetic nanoparticles as contrast agents in magnetic resonance imaging and radiosensitizers in radiotherapy. In: *Fundamentals and Industrial Applications of Magnetic Nanoparticles.* Elsevier; 2022:291–316.
38. Weissleder R, Pittet MJ. Imaging in the era of molecular oncology. *Nature.* 2008;452(7187):580–589. doi:10.1038/nature06917
39. Fu Q, Zhu R, Song J, Yang H, Chen X. Photoacoustic imaging: contrast agents and their biomedical applications. *Adv Mater.* 2019;31(6):e1805875. doi:10.1002/adma.201805875
40. Attia ABE, Balasundaram G, Moothanchery M, et al. A review of clinical photoacoustic imaging: current and future trends. *Photoacoustics.* 2019;16:100144. doi:10.1016/j.pacs.2019.100144
41. Wang B, Hai J, Wang Q, Li T, Yang Z. Coupling of luminescent terbium complexes to Fe₃O₄ nanoparticles for imaging applications. *Angew Chem Int Ed Eng.* 2011;50(13):3063–3066. doi:10.1002/anie.201006195
42. Gao L, Zhuang J, Nie L, et al. Intrinsic peroxidase-like activity of ferromagnetic nanoparticles. *Nat Nanotechnol.* 2007;2(9):577–583. doi:10.1038/nnano.2007.260
43. Cohen-Sela E, Chorny M, Koroukhov N, Danenberg HD, Golomb G. A new double emulsion solvent diffusion technique for encapsulating hydrophilic molecules in PLGA nanoparticles. *J Control Release.* 2009;133(2):90–95. doi:10.1016/j.jconrel.2008.09.073
44. Yang Q, Li P, Ran H, et al. Polypyrrole-coated phase-change liquid perfluorocarbon nanoparticles for the visualized photothermal-chemotherapy of breast cancer. *Acta Biomater.* 2019;90:337–349. doi:10.1016/j.actbio.2019.03.056
45. Cao Y, Chen Y, Yu T, et al. Drug release from phase-changeable nanodroplets triggered by low-intensity focused ultrasound. *Theranostics.* 2018;8(5):1327–1339. doi:10.7150/thno.21492
46. Huang Y, He S, Cao W, Cai K, Liang XJ. Biomedical nanomaterials for imaging-guided cancer therapy. *Nanoscale.* 2012;4(20):6135–6149. doi:10.1039/c2nr31715j
47. Jiang X, Han Y, Zhang H, et al. Cu-Fe-Se ternary nanosheet-based drug delivery carrier for multimodal imaging and combined chemo/photothermal therapy of cancer. *ACS Appl Mater Interfaces.* 2018;10(50):43396–43404. doi:10.1021/acsami.8b15064
48. Chen J, Ding J, Wang Y, et al. Sequentially responsive shell-stacked nanoparticles for deep penetration into solid tumors. *Adv Mater.* 2017;29(32). doi:10.1002/adma.201701170
49. Kim J, Jo C, Lim WG, et al. Programmed nanoparticle-loaded nanoparticles for deep-penetrating 3D cancer therapy. *Adv Mater.* 2018;e1707557. doi:10.1002/adma.201707557

International Journal of Nanomedicine

Dovepress

Publish your work in this journal

The International Journal of Nanomedicine is an international, peer-reviewed journal focusing on the application of nanotechnology in diagnostics, therapeutics, and drug delivery systems throughout the biomedical field. This journal is indexed on PubMed Central, MedLine, CAS, SciSearch®, Current Contents®/Clinical Medicine, Journal Citation Reports/Science Edition, EMBase, Scopus and the Elsevier Bibliographic databases. The manuscript management system is completely online and includes a very quick and fair peer-review system, which is all easy to use. Visit <http://www.dovepress.com/testimonials.php> to read real quotes from published authors.

Submit your manuscript here: <https://www.dovepress.com/international-journal-of-nanomedicine-journal>